

Tunable Topological Phases in an Organic One-Dimensional Mott Chain: Odd-Haldane ($S = 1/2$) and Haldane ($S = 1$)

Khalid N. Anindya*¹ and Hong Guo¹

¹Department of Physics, McGill University, Montréal, QC H3A 2T8, Canada

*Email: khalid.anindya@mcgill.ca

Abstract

Establishing symmetry-protected topological (SPT) phases with interactions in chemically realistic systems remains an open challenge. We show that a single, synthetically plausible organic one-dimensional chain, tunable via chemical modification of its radical sites, hosts two such phases: an odd-Haldane phase of a dimerized $S = \frac{1}{2}$ Heisenberg chain and a Haldane phase of an $S = 1$ chain realized when Hund coupling locks two $S = \frac{1}{2}$ spins per monomer into $S = 1$. Density-functional theory places the active manifold deep in the Mott regime ($U/t \approx 126$), justifying a spin-only Heisenberg description; a compact $(t, U) \rightarrow J$ mapping then fixes exchange couplings. Exact diagonalization and DMRG reveal a consistent SPT fingerprint across both phases, including a quantized many-body Zak phase, even-degenerate entanglement spectrum, protected edge spins, and characteristic triplon/Haldane features in $S^{+-}(q, \omega)$. Our results identify a chemically programmable molecular platform for interacting SPT physics in one dimension and suggest concrete spectroscopic routes to organic Haldane spin chains for nanoscale quantum devices.

Keywords

Symmetry-protected topological phases; Haldane phase; Dimerized spin chain; Magnetic Nanographene; Many-body Zak phase

Carbonyl-triphenyl (CTP) derivatives offer a rigid, planar π -framework with orthogonal chemical handles (carbonyls, N-heteroatoms) that enable stable π -radicals and on-surface covalent coupling. High-spin aza-triangulene molecules derived from CTP-like precursors have been synthesized and characterized at the single-molecule level,^{1,2} and closely related radical motifs have been stabilized in extended two-dimensional π -networks such as Kagome graphene,³ establishing the feasibility of embedding robust spins in covalently bonded lattices. More broadly, on-surface synthesis of open-shell nanographenes and diradical frameworks now enables exchange pathways, lattice geometry, and symmetry to be engineered at the atomic scale, realizing designer spin models in organic π -systems.⁴⁻⁹ Together with nanographene spin chains that already control chain length, parity, termination, and access spin excitations spectroscopically,^{4,5} these advances

motivate a 1D CTP-based polymer whose topological character and edge multiplets can be tuned *chemically*, providing a realistic route toward edge-spin qubits and topological spin-transport building blocks.¹⁰⁻¹²

From a band-structure perspective, the two spin-chain realizations we target are natural interacting analogues of well-known electronic models. The dimerized spin- $\frac{1}{2}$ “odd-Haldane” chain is the spin counterpart of the topological Su–Schrieffer–Heeger (SSH) polyacetylene chain: strong and weak bonds alternate, and the topological sector is selected by which bond is cut at the ends.^{13,14} In the SSH model, dimerization of hopping amplitudes produces a quantized Zak phase and midgap boundary states for one choice of termination; in the odd-Haldane chain, dimerization of antiferromagnetic exchanges produces a quantized many-body Zak phase and fractional $S = \frac{1}{2}$ edge spins for the bond-centred (“odd”)

dimerization pattern.^{4,5,15} By contrast, a spin-1 Haldane chain is uniform in real space but topological in its *entanglement*: it supports non-local string order and $S = \frac{1}{2}$ edge modes even without explicit dimerization, as captured in the AKLT valence-bond picture.¹⁵⁻¹⁸ Here we show that a single, synthetically plausible CTP-based chain realizes both situations within a single chemical backbone: an SSH-like, bond-centred odd-Haldane phase for a spin- $\frac{1}{2}$ radical chain, and a site-centred Haldane phase for a Hund-coupled spin-1 superatom chain.

Interacting symmetry-protected topological (SPT) phases in one dimension are distinguished by non-local order and boundary excitations that are robust against local perturbations preserving the protecting symmetries.¹⁵⁻²¹ In the present CTP-based chain, two archetypes emerge from distinct radicalization patterns on the same molecular scaffold: a single π -radical per monomer yields an $S=\frac{1}{2}$ lattice with $J_1 \ll J_2$ (odd-Haldane), whereas two radicals on the same monomer undergo strong ferromagnetic locking by Hund-coupling ($J_1 < 0$, $|J_1| \gg J_2$), forming $S=1$ superatoms (Haldane) coupled antiferromagnetically by J_2 . Both chains are centrosymmetric, but the inversion center differs, *site-centred* for $S=1$ and *bond-centred* for $S=\frac{1}{2}$, which fixes the Zak-phase origin and governs termination-dependent edge multiplets.¹⁵

Because band-structure proxies do not apply in interacting 1D systems and finite samples have edges and terminations, we establish SPT order using experiment-facing many-body diagnostics: a quantized many-body Zak/polarization phase, an even-degenerate entanglement spectrum at symmetry-respecting cuts, termination-dependent ground-state multiplets, and real-space edge magnetization with an exponential envelope.^{15,20-24} A key advantage of our platform is comparability: both phases arise from the *same* molecular backbone and protecting symmetries, differing only in intra-unit exchange, which allows an apples-to-apples assessment within one chemistry. We focus on two complementary low-energy descriptions. First, the alternating-exchange Heisenberg (AEH) chain for a radical $S = \frac{1}{2}$ lattice,

$$H_{\text{AEH}} = \sum_{j=1}^{L/2} [J_1 \mathbf{S}_{2j-1} \cdot \mathbf{S}_{2j} + J_2 \mathbf{S}_{2j} \cdot \mathbf{S}_{2j+1}], \quad (1)$$

with $J_2 > J_1 \geq 0$ realizing the odd-Haldane SPT in the strongly dimerized limit. For open chains, which bond is cut selects the SPT sector:^{4,5} cutting a weak bond (J_1) yields an even-Haldane termination with two $S = \frac{1}{2}$ edge modes and a near-fourfold ground-state manifold in long chains; cutting

a strong bond (J_2) removes free edges (trivial ground state); and mixed terminations give a twofold manifold with a single edge mode.⁵ In the bulk, J_2 pins singlets and the elementary excitation is a dispersive one-triplon branch with a cosine-like shape,^{5,25} whose open-boundary folding and intensity ridge have been identified in atomically precise organic chains.

Second, in the Hund-coupled case two $S = \frac{1}{2}$ on each monomer bind ferromagnetically ($J_1 < 0$, $|J_1| \gg J_2$) into a rigid $S=1$ superatom. Projecting the inter-monomer coupling onto the triplet subspace gives an *effective* antiferromagnetic $S=1$ chain with exchange set by the inter-monomer bridges (proportional to J_2). This uniform $S=1$ chain realizes the Haldane phase: a finite bulk gap and $S = \frac{1}{2}$ edge states under open boundaries, yielding a near-fourfold ground-state manifold in long chains that is independent of how the chain is cut.¹⁵⁻¹⁹

Finally, periodic electronic-structure calculations place the active manifold deep in the Mott regime, validating a spin-only Heisenberg mapping for *both* realizations. As a dynamical fingerprint we compute $S^{+-}(q, \omega)$: it shows (i) a single triplon branch with bandwidth consistent with J_1 in the dimerized $S = \frac{1}{2}$ case and (ii) the Haldane magnon with gap and bandwidth set by the effective inter-monomer antiferromagnetic exchange in the $S = 1$ case; open-chain Fourier maps reproduce these ridges with the expected folding, in line with previous studies on different haldane chains.²⁶⁻²⁹ Detailed explanation regarding the numerical treatment of the spin chains has been provided in the supporting information (SI) section.

Results and discussion

Chain chemistry and dimerized $S = 1/2$ spin chain

Figure 1 summarizes the chemical design and spin texture of the nanographene spin-1/2 chain. The building block is an N-doped carbonyl-triphenyl (CTP) core (Fig. 1a, left). Upon suitable functionalization, one peripheral site is converted into a stable $S = 1/2$ radical (middle), yielding a single unpaired spin largely confined to each N-doped CTP backbone. Such site-selective radicalization of the same N-doped CTP motif has been demonstrated for isolated molecules¹ and for its two-dimensional Kagome lattice on Au(111), where only a specific carbonyl site hosts the radical.³ Here we exploit this selectivity to stitch the radicals into a one-dimensional chain (right), where neighboring spin centers are cou-

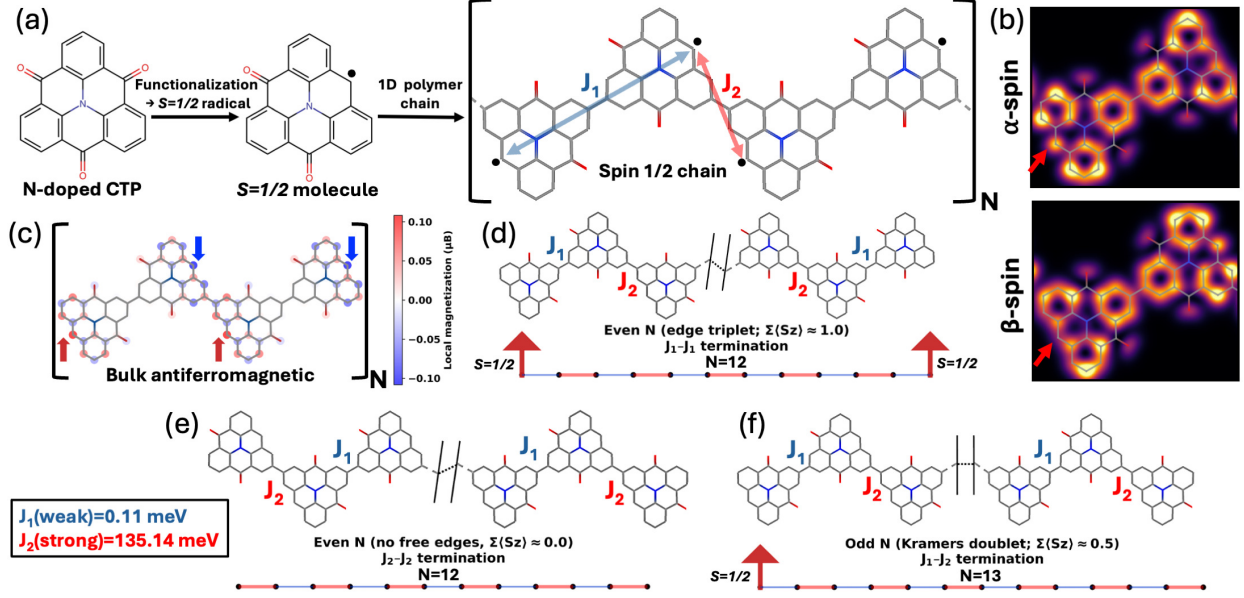


Figure 1: Chain chemistry and terminations of the dimerized nanographene spin-1/2 chain. (a) Chemical route from N-doped CTP to a stable $S = 1/2$ radical and its one-dimensional polymer, whose magnetic backbone is an alternating-exchange spin-1/2 chain with couplings J_1 (blue) and J_2 (red). (b) Simulated spin-polarized STM constant-current maps for the isolated radical (top: α -spin, bottom: β -spin), showing complementary contrast at the same molecular site (red arrows), consistent with a single $S = 1/2$ ground state. (c) DFT+ U local magnetization for a polymer segment, revealing bulk antiferromagnetic order with alternating up/down monomer moments. (d-f) Schematic open chains with different terminations. J_1 - J_1 : two $S = 1/2$ edge spins forming an edge triplet ($\sum_i \langle S_i^z \rangle \approx 1$). J_2 - J_2 : intact strong dimers and no free edges ($\sum_i \langle S_i^z \rangle \approx 0$). Mixed J_1 - J_2 : a single unpaired edge spin giving a Kramers doublet ($\sum_i \langle S_i^z \rangle \approx 1/2$).

pled along a single π -conjugated backbone but connected by two symmetry-inequivalent bridges, realizing an alternating-exchange Heisenberg chain with weak bond J_1 and strong bond J_2 .

To visualize the spin texture, we compute spin-resolved LDOS maps within a DFT+ U -based Tersoff-Hamann approximation.³⁰ The simulated spin-polarized STM images in Fig. 1b show α - and β -spin contrast that is complementary and localized at the radical site (red arrows), consistent with a spin-split frontier orbital. When the radicals are assembled into the polymer, DFT+ U calculations reveal a bulk antiferromagnetic configuration with alternating monomer moments (Fig. 1c); the color scale highlights small but finite spin polarization around the radical sites, reflecting the delocalized π character of the spin-1/2 state.

Mapping DFT+ U total energies onto the Heisenberg model yields $J_1 \approx 0.11$ meV and $J_2 \approx 135$ meV (see SI section S2), placing the chain extremely close to the ideal limit of isolated antiferromagnetic dimers. The termination then controls the edge-state manifold. For an even- N chain with J_1 - J_1 termination

(Fig. 1d), both ends cut weak bonds and leave two $S = 1/2$ edge spins forming an edge triplet with $\sum_i \langle S_i^z \rangle \approx 1$. For an even- N chain with J_2 - J_2 termination (Fig. 1e), all strong dimers remain intact and $\sum_i \langle S_i^z \rangle \approx 0$. An odd- N chain with mixed J_1 - J_2 termination (Fig. 1f) hosts a single unpaired edge spin and realizes a Kramers doublet with $\sum_i \langle S_i^z \rangle \approx 1/2$. These three terminations provide a direct chemical handle on the edge states of the dimerized spin-1/2 chain.

Topological fingerprints and edge multiplets of the dimerized $S = 1/2$ chain

The different terminations of the nanographene spin-1/2 chain lead to distinct bulk topologies and edge-state manifolds, which we diagnose using many-body Zak phases, entanglement spectra, and spin-resolved multiplet structures (Fig. 2). For each geometry we impose a twist ϕ on the periodic bond and follow the ground state $|\psi_0(\phi)\rangle$ around a loop $0 \leq \phi < 2\pi$. The local Berry angles between neighboring twists and their cumulative sum Zak(ϕ) [Fig. 2a] yield a quan-

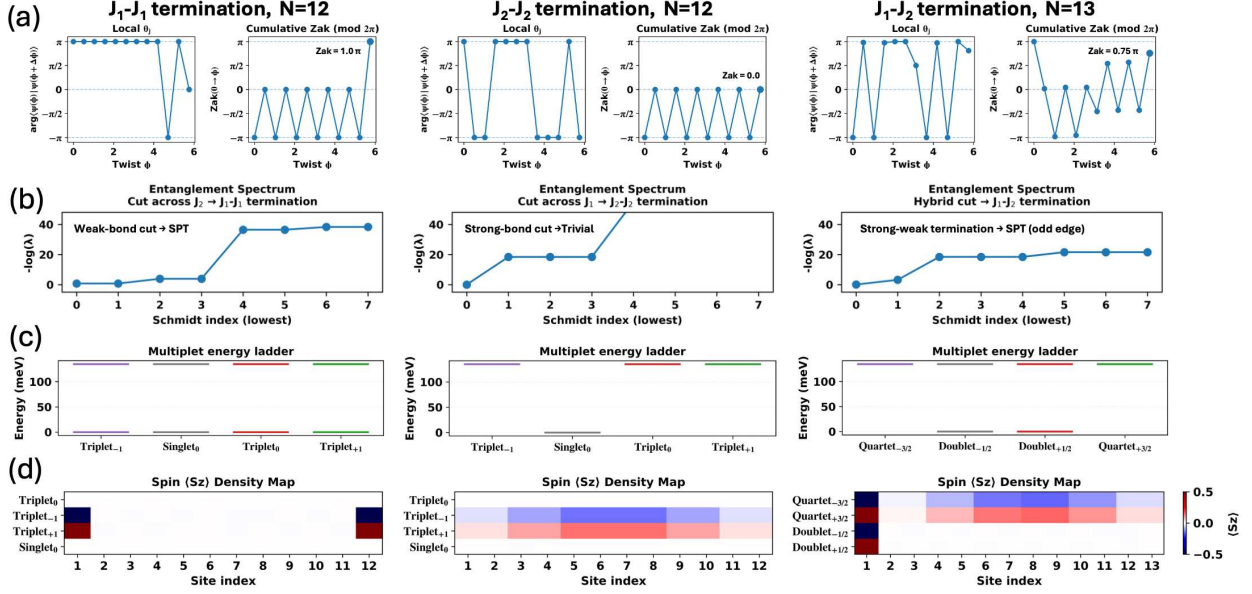


Figure 2: Topological diagnostics of the dimerized nanographene spin-1/2 chain. (a) Many-body Zak phase from twisted boundary conditions. J_1 - J_1 (even N) gives π (SPT), J_2 - J_2 (even N) gives 0 (trivial), and mixed J_1 - J_2 (odd N) yields $\sim 0.75\pi$, consistent with a single fractional edge spin-1/2. (b) Entanglement spectra $-\log \lambda$ versus Schmidt index (with λ the eigenvalues of the reduced density matrix) for cuts across weak (J_1) and strong (J_2) bonds. Weak-bond cuts in J_1 - J_1 and J_1 - J_2 chains show a nearly fourfold-degenerate lowest manifold (SPT), whereas a strong-bond cut in J_2 - J_2 chains yields a non-degenerate spectrum (trivial). (c) Low-energy multiplet ladders from ED: J_1 - J_1 has a triplet ground state (two correlated edge spins), J_2 - J_2 a singlet (no free edges), and odd- N J_1 - J_2 a Kramers doublet (single edge spin-1/2). (d) Spin-density maps $\langle S_i^z \rangle$ for the lowest multiplets, highlighting two edge-localized $S = 1/2$ moments in J_1 - J_1 , no edge polarization in J_2 - J_2 , and a single edge $S = 1/2$ in J_1 - J_2 .

tized many-body Zak phase modulo 2π . An even- N chain with J_1 - J_1 termination has Zak phase π , consistent with an interacting SPT phase protected by inversion and spin-rotation symmetries, whereas the even- N J_2 - J_2 chain is trivial with Zak phase 0. For the odd- N chain with mixed J_1 - J_2 termination, the cumulative phase saturates near $\sim 0.75\pi$, reflecting finite-size fractionalization of a single edge spin-1/2.

The entanglement spectra (ES) [Fig. 2b], obtained as $-\log \lambda_n$ from the eigenvalues $\{\lambda_n\}$ of the reduced density matrix for a bipartition, show the same pattern. Cuts across a weak J_1 bond in J_1 - J_1 and J_1 - J_2 chains exhibit a nearly fourfold-degenerate lowest manifold, characteristic of an SPT phase, whereas a strong-bond cut in the J_2 - J_2 chain yields a non-degenerate spectrum typical of a trivial product state. For the odd- N J_1 - J_2 chain, a hybrid cut produces a low-lying pair of near-degenerate levels, consistent with a single unscreened edge spin. The slight deviations from exact fourfold (even- N J_1 - J_1) or twofold (odd- N J_1 - J_2) degeneracy may arise in ES: the bipartition of a finite chain creates two inequivalent vir-

tual edges whose local environments and residual couplings are not strictly symmetric, lifting the degeneracies slightly while preserving the near-degenerate SPT structure.

To connect these bulk diagnostics to real-space edge physics, we classify the low-energy eigenstates into $SU(2)$ multiplets and track their energies [Fig. 2c]. For J_1 - J_1 termination the ground state is a triplet with degenerate singlet and higher triplet partners, reflecting two correlated $S = 1/2$ edge spins. For J_2 - J_2 termination the ground state is a singlet separated from triplet excitations, consistent with all dimers paired into a trivial bulk state. The odd- N J_1 - J_2 chain shows a Kramers doublet ground state followed by quartet and higher multiplets, corresponding to a single fractional edge spin-1/2.

Finally, spin-resolved density maps for the lowest multiplets [Fig. 2d] make the edge localization explicit. In the J_1 - J_1 geometry the triplet components show strong, opposite magnetizations pinned at the two chain ends, with negligible bulk magnetization. For J_2 - J_2 the spin density is small and nearly uni-

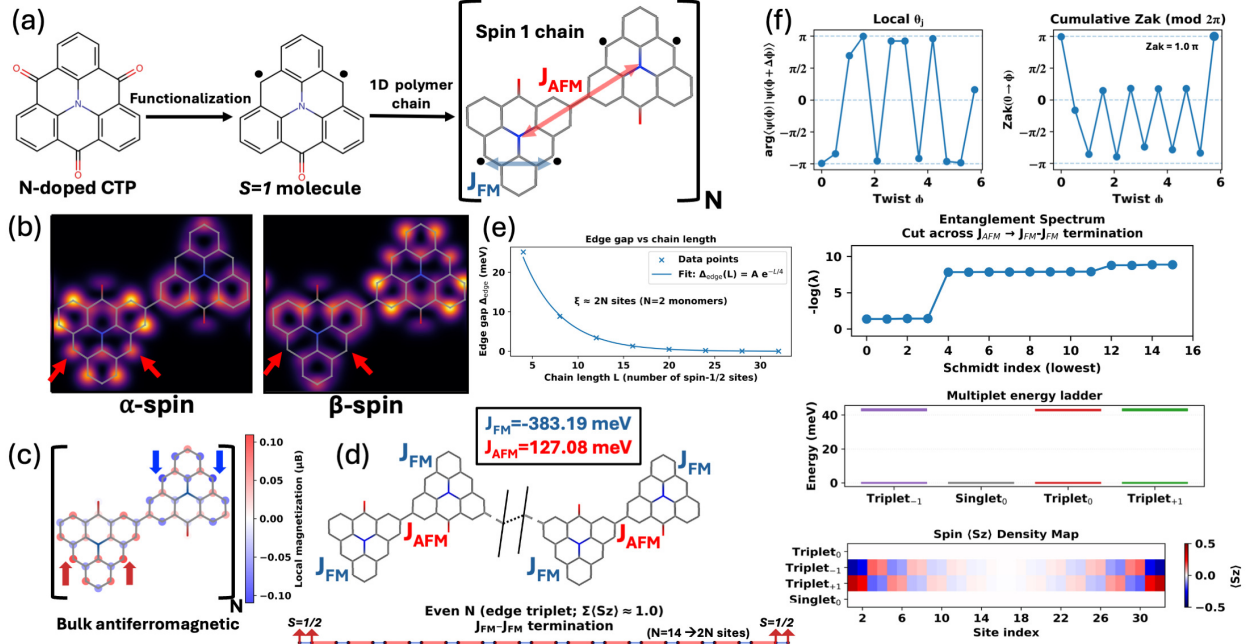


Figure 3: Spin-1 Hund chain from N-doped CTP superatoms and its Haldane signatures. (a) Chemical route from N-doped CTP to an $S = 1$ Hund monomer and its one-dimensional polymer, with intra-monomer ferromagnetic J_{FM} and inter-monomer antiferromagnetic J_{AFM} couplings defining the spin-1 chain. (b) Simulated spin-resolved STM image of the isolated $S = 1$ monomer, showing complementary α - and β -spin contrast at the two radical sites (red arrows). (c) DFT+ U local magnetization for a polymer segment, revealing bulk antiferromagnetic order with alternating monomer moments. (d) Even- N open chain with J_{FM} - J_{FM} termination and the corresponding spin-1/2 lattice cartoon, exposing two edge $S = 1/2$ moments that form an edge triplet. (e) Edge-triplet splitting $\Delta_{\text{edge}}(L)$ versus chain length L with an exponential fit $\Delta_{\text{edge}}(L) = A \exp(-L/\xi)$, yielding a short correlation length of order two spin-1 monomers. (f) DMRG diagnostics: many-body Zak phase quantized to π , a nearly fourfold-degenerate entanglement/multiplet manifold, and spin-density maps $\langle S_i^z \rangle$ showing two localized $S = 1/2$ edge spins with a slight intra-monomer asymmetry.

form, with no pronounced edge polarization. In the odd- N J_1 - J_2 chain the ground-state doublet exhibits a localized spin-1/2 at a single end of the chain, realizing the expected fractional edge excitation of an SPT phase with an odd number of dimers. Together, these diagnostics establish that weak-bond terminations realize an interacting SPT phase with protected edge spins, while strong-bond terminations are topologically trivial.

Hund-coupled spin-1 chain and Haldane edge states

We now turn to the spin-1 chain realized by Hund-coupled superatoms built from the same N-doped CTP motif. As sketched in Fig. 3a, a different functionalization stabilizes two radical sites on each molecule, which are ferromagnetically locked by an intra-molecular exchange $J_{FM} < 0$ and form an $S = 1$

“Hund monomer”. Stitching these units into a one-dimensional polymer produces a spin-1 chain in which neighboring monomers are coupled antiferromagnetically by $J_{AFM} > 0$, i.e. a J_{FM} - J_{AFM} alternating Heisenberg chain where the monomer acts as a superatom rather than a rigid atomic $S = 1$ ion.

The local spin texture of the $S = 1$ monomer is visualized in Fig. 3b via computed spin-resolved LDOS maps. The simulated α - and β -spin STM images show complementary contrast at the two radical sites (red arrows), consistent with a pair of ferromagnetically aligned $S = 1/2$ moments. In the polymer, DFT+ U calculations reveal a bulk antiferromagnetic configuration with alternating monomer magnetizations and a small but finite spin polarization extending over the molecular rings (Fig. 3c). Mapping collinear DFT+ U energies onto the spin model yields a large intra-monomer ferromagnetic exchange $J_{FM} \approx -383$ meV, which locks the two

$S = \frac{1}{2}$ spins on each monomer into a Hund-coupled triplet, and an antiferromagnetic inter-monomer coupling $J_{\text{AFM}} \approx 127$ meV (Fig. 3d), so $|J_{\text{FM}}| \gg J_{\text{AFM}}$ and the system lies deep in the Haldane regime of a spin-1 chain built from Hund-coupled superatoms.

Open chains with an even number of monomers and a $J_{\text{FM}}-J_{\text{FM}}$ termination (Fig. 3d) preserve the ferromagnetic dimers at both ends and cut only antiferromagnetic bonds. This exposes the characteristic $S = 1/2$ edge spins of the Haldane phase: the lowest states form an edge triplet whose $S^z = +1$ component has $\sum_i \langle S_i^z \rangle \approx 1$, while the bulk magnetization is negligible. Because the two $S = 1/2$ moments are chemically bound within the same monomer, the chain can only be terminated between monomers; cutting the intra-monomer bond would break the molecule. Thus both even- and odd-length chains always end on intact $S = 1$ monomers and are topologically equivalent: any realistic termination exposes the same pair of fractional $S = 1/2$ edge spins. The finite-size splitting of this edge triplet, $\Delta_{\text{edge}}(L)$, decays exponentially with chain length L , as shown in Fig. 3e; a fit $\Delta_{\text{edge}}(L) = A \exp(-L/\xi)$ yields a correlation length $\xi \simeq 2N$ sites (about two spin-1 monomers), confirming that relatively short chains already capture the asymptotic Haldane edge physics.

DMRG calculations³¹ on longer chains provide the many-body topological diagnostics summarized in Fig. 3f. The many-body Zak phase obtained from twisted boundary conditions quantizes to π , signalling an interacting SPT phase protected by inversion and spin-rotation symmetries, and the entanglement spectrum shows a nearly fourfold-degenerate lowest manifold when the cut is placed across the monomers, as expected for a spin-1 Haldane chain. The low-energy multiplet ladder and spin-density maps (Fig. 3f, middle and bottom) reveal a triplet ground state with two localized $S = 1/2$ edge spins at opposite ends. Each pair of neighboring sites in the spin-density map corresponds to the two ferromagnetically locked $S = 1/2$ moments of a single Hund monomer; in the open chain their individual $\langle S_i^z \rangle$ values differ slightly because the site facing the inter-monomer antiferromagnetic bond is more strongly entangled with the neighbor, so finite $|J_{\text{FM}}|/J_{\text{AFM}}$ and boundary effects break the internal symmetry. This slight intra-monomer imbalance is in fact a key strength of our microscopic description: by keeping two spin-1/2 sites and using the alternating Heisenberg Hamiltonian rather than a coarse-grained spin-1 model, we resolve the internal structure and bonding asymmetry of each Hund monomer and closely mirror the real spin distribution. At the outermost monomers the pair-summed spin density is close to

$\pm 1/2$, identifying the fractional edge $S = 1/2$ modes of the Haldane phase, while interior monomers carry only a small residual net moment.

Hubbard mapping, Mott regime, and triplon dynamics

To connect the *ab initio* electronic structure to the effective spin models, we first analyze the spin-resolved band structures of the spin-1/2 and spin-1 chains in antiferromagnetic (AFM) and ferromagnetic (FM) configurations [Fig. 4a,b]. In both chains the AFM state is insulating with a large single-particle gap around the Fermi level, while the FM configuration shows the same bands strongly spin split (red/blue lines): a single majority-spin band (or pair of bands for the Hund chain) lies closest to E_F , and its dispersion defines the FM bandwidth W_{FM} used to extract t . While single-particle band structures do not by themselves establish interacting SPT order, they provide a compact fingerprint of the real-space connectivity and inversion center that underlie the effective spin models. In the spin-1/2 chain, the radicalized site alternates from one edge of the N-doped CTP monomer to the next, so the effective $S = 1/2$ degrees of freedom are *bond-centered* between monomers; a translation plus inversion about a bond center generates two inequivalent exchanges (J_1, J_2) and visible band folding and small splittings along Γ -Y in Fig. 4a, the electronic fingerprint of the frustrated odd-Haldane geometry. By contrast, in the spin-1 chain the Hund-coupled superatoms are *site-centered* and all AFM links between monomers are symmetry-equivalent, leading to more regular, nearly symmetric AFM and FM band ladders [Fig. 4b] consistent with a uniform site-centered spin-1 Haldane chain.

Following the standard bandwidth scaling of one-band Hubbard mappings,³² we extract the nearest-neighbor hopping t from the FM bandwidth of a single spin channel,

$$W_{\text{FM}} = 2z|t| \Rightarrow |t| = \frac{W_{\text{FM}}}{2z}, \quad (2)$$

$z = 2$ (1D) $\Rightarrow |t| = \frac{W_{\text{FM}}}{4}$. and estimate the effective on-site repulsion from the AFM spectra via

$$U_{\text{eff}} \approx E_g^{\text{AFM}} + W_{\text{AFM}}. \quad (3)$$

These relations give the usual correlation measure U_{eff}/t used to locate the Mott regime in U/t space ($U/t \geq 4.3$).^{33,34} Applying this procedure to the DFT+ U bands in Fig. 4a,b yields $t \approx 12.25$ meV for the spin-1/2 chain and $t \approx 9.82$ meV for the spin-1 chain at 0 K, with an essentially identical

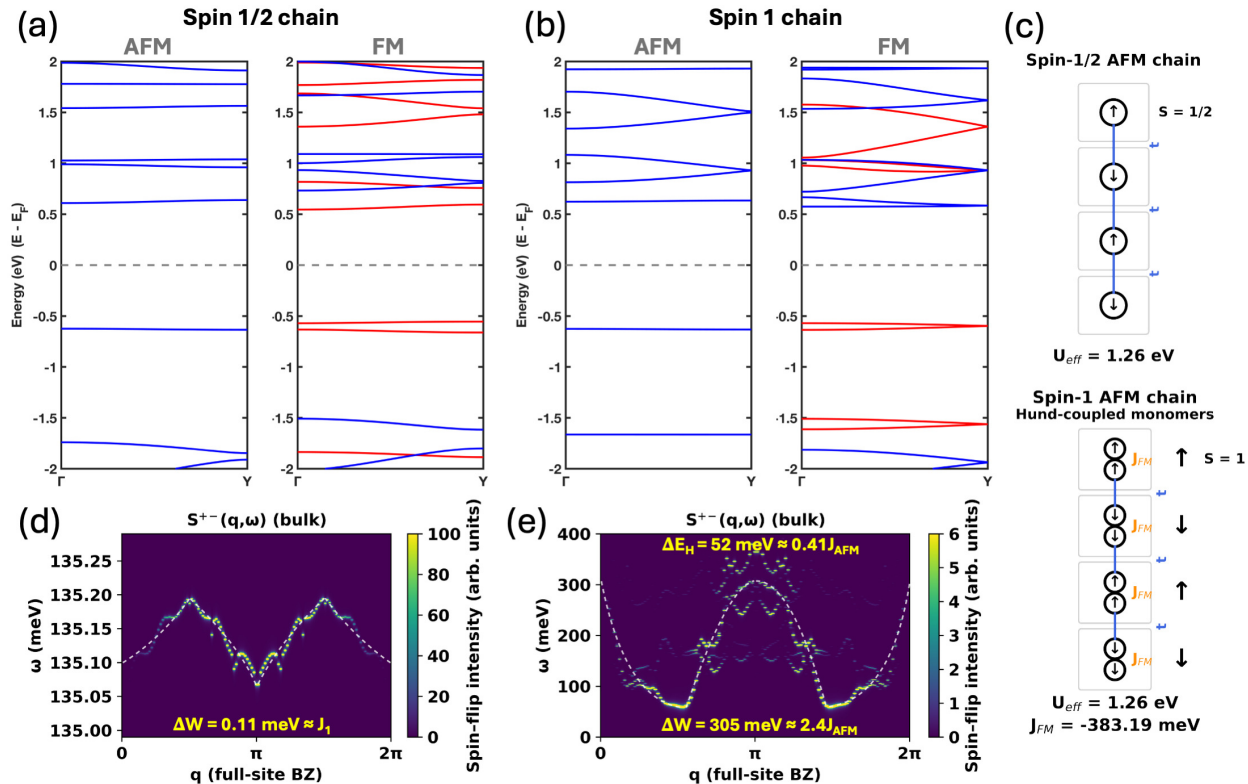


Figure 4: (a,b) Spin-resolved DFT+ U band structures of the spin-1/2 and spin-1 chains in AFM (left) and FM (right) configurations (blue/red: opposite spins; dashed line: E_F , bands are spin-degenerate in AFM case). (c) One-orbital Hubbard cartoon: the spin-1/2 chain has one half-filled orbital per monomer with a single hopping t and on-site interaction $U_{\text{eff}} = 1.26$ eV, while in the spin-1 chain two ferromagnetically locked orbitals form an $S = 1$ site with the same t and U_{eff} and strong intra-monomer exchange J_{FM} . (d) Bulk $S^{+-}(q, \omega)$ for the dimerized spin-1/2 chain, showing a very narrow W-shaped triplon band with bandwidth $\Delta W \approx 0.11$ meV $\approx J_1$; the dashed line is the one-triplon dispersion of the fitted spin model. (e) $S^{+-}(q, \omega)$ for the spin-1 Hund chain, displaying an M-shaped triplon branch with Haldane gap $\Delta E_H \approx 52$ meV $\approx 0.41 J_{\text{AFM}}$, total bandwidth $\Delta W \approx 305$ meV $\approx 2.4 J_{\text{AFM}}$, and additional weak branches from internal Hund modes; dashed lines again show the one-triplon dispersion.

$U_{\text{eff}} \approx 1.26$ eV for both. The resulting ratios $U_{\text{eff}}/t \sim 100$ – 130 place both chains deep in the Mott regime, fully justifying the spin-only Heisenberg description. The corresponding parameters at 0 and 300 K are summarized in Table 1.

Panel 4c summarizes the underlying one-band Hubbard picture. For the spin-1/2 chain, each radical monomer is represented by a single half-filled orbital with on-site interaction $U_{\text{eff}} = 1.26$ eV and a single nearest-neighbor hopping t between monomers. In the spin-1 chain, two such orbitals on each monomer are ferromagnetically locked into an effective $S = 1$ superatom, but charge fluctuations between neighboring monomers are still governed by the same scalar hopping t and on-site U_{eff} . Thus both the dimerized spin-1/2 chain and the Hund-coupled spin-1 chain de-

scend from the same fermionic backbone with one effective inter-monomer hopping and a common U_{eff} , differing only in local spin multiplicity and the resulting exchange hierarchy.

To assess thermal robustness, we evolve each chain at 300 K in LAMMPS using SevenNet-MF-ompa machine-learning (ML) interatomic potentials (see SI section S3 and S4),^{35,36} fine-tuned with DFT data for the same molecular family.³⁷ Representative configurations from these molecular-dynamics trajectories are quenched and re-evaluated with the same DFT+ U band-structure and exchange-mapping procedure. The finite-temperature parameters (Table 1) show only modest renormalization: t is reduced by ~ 3 – 5% (from 12.25 to 11.85 meV in the spin-1/2 chain and from 9.82 to 9.74 meV in the spin-1 chain),

Table 1: Exchange parameters, hopping amplitudes, and interaction strengths for the spin-1/2 and spin-1 chains extracted from DFT+ U at 0 and 300 K.

Species	T (K)	J_1 (meV)	J_2 (meV)	Characterization	t (meV)	U (eV)	U/t
Spin 1/2	0	0.11	135.14	Dimerized odd Haldane SPT	12.25	1.26	103
—	300	0.08	136.99	—	11.85	1.26	106
Spin 1	0	-383.19	127.08	Haldane SPT	9.82	1.26	128
—	300	-376.91	62.70	—	9.74	1.26	129

while J_2 changes by less than 2 meV and U_{eff} remains essentially unchanged. Thus, the chains remain deep in the Mott regime, and thermal distortions at 300 K do not drive the system out of the exchange hierarchy and correlation regime that supports the odd-Haldane and Haldane SPT ground states.

Finally, we connect this Hubbard-scale picture to the many-body spin dynamics via the bulk spin-flip structure factor $S^{+-}(q, \omega)$ [Fig. 4d,e]. For the dimerized spin-1/2 chain, $S^{+-}(q, \omega)$ shows a very narrow triplon band with total bandwidth $\Delta W \approx 0.11$ meV, matching the weak inter-dimer coupling J_1 ,²⁷ and displaying a characteristic “W”-shaped dispersion: the band maximum lies near $q \approx \pi/2$ (and $3\pi/2$) and the minima near $q = 0, \pi, 2\pi$, with most spectral weight between 0 and π . This pattern reflects the bond-centered odd-Haldane chain: the elementary triplon lives on a strong J_2 dimer, so the effective dimer lattice has twice the spacing of the site lattice and its AFM wave vector maps to $q \approx \pi/2$ in the full-site Brillouin zone, while form-factor cancellations suppress weight at $q = 0, \pi$. In contrast, the Hund-coupled spin-1 chain displays a broad triplon branch with an “M”-shaped dispersion: the band minimum lies near $q \approx \pi/2$, the maxima occur near $q \approx 0$ and π , the Haldane gap at the minimum is $\Delta E_H \approx 52$ meV $\simeq 0.41 J_{\text{AFM}}$, and the total bandwidth $\Delta W \approx 305$ meV is of order $2.4 J_{\text{AFM}}$.^{28,29} Additional, weaker branches at higher energies reflect secondary triplon modes associated with the internal Hund-coupled structure, underscoring that the chain is not a perfectly rigid spin-1 model but a molecular superatom realization. The dashed ridges overlaying both intensity maps are the one-triplon dispersions obtained from the ED spin models with J_{FM} and J_{AFM} fitted to DFT+ U , demonstrating quantitative agreement between the microscopic Hubbard-scale description and the emergent triplon dynamics.

Conclusions

We have shown that a single N-doped carbonyl-triphenyl platform can host two distinct interacting SPT phases in one dimension: a bond-centered,

dimerized spin-1/2 odd-Haldane chain and a site-centered spin-1 Haldane chain built from Hund-coupled superatoms. Spin-polarized DFT+ U combined with exchange mapping, ED, DMRG, and $S^{+-}(q, \omega)$ demonstrates that both systems lie deep in the Mott regime, exhibit fractional $S = 1/2$ edge modes, and display characteristic W- and M-shaped triplon bands in quantitative agreement with fitted Heisenberg models. ML-accelerated finite-temperature calculations further show that J_1 , J_2 , t , and U_{eff} are only weakly renormalized at 300 K, indicating that the microscopic exchange hierarchy and correlation regime underpinning the SPT ground states is stable against thermal distortions up to room temperature and broadly promising as chemically programmable platforms for edge-spin qubits, topological spin transport, and quantum simulation of interacting SPT phases.

Methods

The effective spin models are isotropic Heisenberg chains and are therefore SU(2) symmetric at zero field.^{38,39} In practice we work in fixed S_{tot}^z sectors and verify a posteriori that the low-lying states form nearly degenerate SU(2) multiplets by monitoring $\langle \hat{S}_{\text{tot}}^2 \rangle$ for the corresponding eigenstates.

For the strongly dimerized spin-1/2 alternating-exchange chain relevant to the nanographene edge segments, the intra-monomer coupling is effectively vanishing, $J_1 \approx 0$, so the system is close to perfectly isolated antiferromagnetic dimers. The correlation length is then only a few lattice sites, and a chain of $N = 12$ monomers already eliminates noticeable finite-size effects: exact diagonalization (ED) on this size yields converged gaps and one-triplon dispersions indistinguishable, within numerical accuracy, from longer chains. In contrast, for the effective spin-1 chain realized by Hund-coupled superatoms the intra-monomer ferromagnetic exchange is large but finite, $|J_1| \gg J_2$, so the monomers are not ideal rigid $S = 1$ atoms and the Haldane edge states extend over several units. To capture this we study chains of $N = 32$ spin-1/2 sites (16 Hund monomers), treated

with density-matrix renormalization group (DMRG) using the TenPy library and exploiting only the U(1) symmetry associated with S_{tot}^z . ED on short chains and DMRG on longer ones provide consistent edge gaps, bulk gaps, and triplon dispersions.

The dynamical spin structure factor $S^{+-}(q, \omega)$ is computed on periodic chains via a Lanczos continued-fraction evaluation of the zero-temperature correlation function, starting from the exact ground state and acting with $\hat{S}_q^+ = N^{-1/2} \sum_j e^{-iqj} (\hat{S}_j^x + i\hat{S}_j^y)$. The resulting intensity maps capture the bulk triplon bands and their dependence on the microscopic couplings, and are the theoretical counterparts of spin-flip features in STM/STS and magnon branches in inelastic neutron scattering.^{40,41}

The exchange parameters J_1 and J_2 are obtained by mapping collinear spin-polarized DFT+ U total energies. All energies entering this mapping are computed with element-resolved Hubbard corrections on the C, N, and O sites of the CTP backbone,³ determined from first-principles linear-response calculations in which small on-site potential shifts are applied and the induced changes in orbital occupations are fitted.⁴² This treatment is particularly important for the localized carbonyl O $2p$ states, which are sensitive to self-interaction errors and control the local moments and exchange splittings.

For the spin-1/2 alternating-exchange chain, each monomer hosts a single localized $S = 1/2$ moment and the low-energy physics is described by two antiferromagnetic couplings $J_1, J_2 > 0$ along the chain. We construct a four-site supercell and evaluate the DFT energies of several collinear configurations ($\uparrow\uparrow | \uparrow\uparrow, \uparrow\downarrow | \uparrow\downarrow, \uparrow\uparrow | \downarrow\downarrow$, etc.). Expressing these energies in terms of $\langle \mathbf{S}_i \mathbf{S}_j \rangle = \pm \frac{1}{4}$ for each bond and solving the resulting linear system yields J_1 (the weaker bond) and J_2 (the stronger bond); in our nanographene chain we find $J_1 \simeq 0$ and $J_2 > 0$, placing the system very close to the ideal dimer limit. For the effective spin-1 chain realized by Hund-coupled superatoms, each monomer hosts two ferromagnetically locked $S = 1/2$ moments. The intra-monomer splitting between FM and AFM alignment defines a large ferromagnetic Hund exchange $J_{\text{FM}} < 0$, while the energy difference between parallel and antiparallel alignment of neighboring monomers in a two-monomer cell defines an antiferromagnetic inter-monomer exchange $J_{\text{AFM}} > 0$. In the spin-1 description we therefore identify

$$J_1 = J_{\text{FM}}, \quad J_2 = J_{\text{AFM}} \equiv J_{\text{eff}}, \quad (4)$$

where J_{eff} is the effective antiferromagnetic coupling between neighboring Hund-coupled $S = 1$ super-

atoms that sets the Haldane gap and triplon bandwidth. Further details of the methods are described in the SI section.

References

- [1] Wang, T.; Berdonces-Layunta, A.; Friedrich, N.; Vilas-Varela, M.; Calupitan, J. P.; Pascual, J. I.; Peña, D.; Casanova, D.; Corso, M.; de Oteyza, D. G. Aza-Triangulene: On-Surface Synthesis and Electronic and Magnetic Properties. *J. Am. Chem. Soc.* **2022**, *144*, 4522–4529.
- [2] Calupitan, J. P.; Berdonces-Layunta, A.; Aguilar-Galindo, F.; Vilas-Varela, M.; Peña, D.; Casanova, D.; Corso, M.; de Oteyza, D. G.; Wang, T. Emergence of π -Magnetism in Fused Aza-Triangulenes: Symmetry and Charge Transfer Effects. *Nano Lett.* **2023**, *23*, 9832–9840.
- [3] Pawlak, R.; Anindya, K. N.; Chahib, O.; Liu, J.-C.; Hiret, P.; Marot, L.; Luzet, V.; Palmino, F.; Chérioux, F.; Rochefort, A.; Meyer, E. On-Surface Synthesis and Characterization of Radical Spins in Kagome Graphene. *ACS Nano* **2025**, *19*, 4768–4777.
- [4] Mishra, S.; Catarina, G.; Wu, F.; Ortiz, R.; Jacob, D.; Eimre, K.; Ma, J.; Pignedoli, C. A.; Feng, X.; Ruffieux, P.; Fernández-Rossier, J.; Fasel, R. Observation of fractional edge excitations in nanographene spin chains. *Nature* **2021**, *598*, 287–292.
- [5] Zhao, C.; Catarina, G.; Zhang, J.-J.; Henriques, J. C. G.; Yang, L.; Ma, J.; Feng, X.; Gröning, O.; Ruffieux, P.; Fernández-Rossier, J.; Fasel, R. Tunable topological phases in nanographene-based spin-1/2 alternating-exchange Heisenberg chains. *Nat. Nanotechnol.* **2024**, Advance online publication.
- [6] Henriques, J.; Ferri-Cortés, M.; Fernández-Rossier, J. Designer Spin Models in Tunable Two-Dimensional Nanographene Lattices. *Nano Lett.* **2024**, *24*, 3355–3360.
- [7] Henriques, J.; Jacob, D.; Molina-Sánchez, A.; Catarina, G.; Costa, A.; Fernández-Rossier, J. Beyond Spin Models in Orbitally Degenerate Open-Shell Nanographenes. *Nano Lett.* **2024**, *24*, 12928–12934.
- [8] Lawrence, J.; Brandimarte, P.; Berdonces-Layunta, A.; Mohammed, M. S. G.; Grewal, A.; Leon, C. C.; Sánchez-Portal, D.;

- de Oteyza, D. G. Probing the Magnetism of Topological End States in 5-Armchair Graphene Nanoribbons. *ACS Nano* **2020**, *14*, 4499–4508.
- [9] Friedrich, N.; Menchón, R. E.; Pozo, I.; Hieulle, J.; Vegliante, A.; Li, J.; Sánchez-Portal, D.; Peña, D.; Garcia-Lekue, A.; Pascual, J. I. Addressing Electron Spins Embedded in Metallic Graphene Nanoribbons. *ACS Nano* **2022**, *16*, 14819–14826.
- [10] Else, D. V.; Schwarz, I.; Bartlett, S. D.; Doherty, A. C. Symmetry-Protected Phases for Measurement-Based Quantum Computation. *Physical Review Letters* **2012**, *108*, 240505.
- [11] Bartlett, S. D.; Brennen, G. K.; Miyake, A.; Renes, J. M. Quantum Computational Renormalization in the Haldane Phase. *Physical Review Letters* **2010**, *105*, 110502.
- [12] Mei, F.; Chen, G.; Tian, L.; Zhu, S.-L.; Jia, S. Robust quantum state transfer via topological edge states in superconducting qubit chains. *Phys. Rev. A* **2018**, *98*, 012331.
- [13] Su, W. P.; Schrieffer, J. R.; Heeger, A. J. Solitons in Polyacetylene. *Phys. Rev. Lett.* **1979**, *42*, 1698–1701.
- [14] Heeger, A. J.; Kivelson, S.; Schrieffer, J. R.; Su, W. P. Solitons in Conducting Polymers. *Rev. Mod. Phys.* **1988**, *60*, 781–850.
- [15] Pollmann, F.; Berg, E.; Turner, A. M.; Oshikawa, M. Symmetry protection of topological phases in one-dimensional quantum spin systems. *Phys. Rev. B* **2012**, *85*, 075125.
- [16] Affleck, I.; Kennedy, T.; Lieb, E. H.; Tasaki, H. Rigorous results on valence-bond ground states in antiferromagnets. *Phys. Rev. Lett.* **1987**, *59*, 799–802.
- [17] Affleck, I.; Kennedy, T.; Lieb, E. H.; Tasaki, H. Valence bond ground states in isotropic quantum antiferromagnets. *Commun. Math. Phys.* **1988**, *115*, 477–528.
- [18] Haldane, F. D. M. Nonlinear field theory of large-spin Heisenberg antiferromagnets: semi-classically quantized solitons of the one-dimensional easy-axis Néel state. *Phys. Rev. Lett.* **1983**, *50*, 1153–1156.
- [19] Haldane, F. D. M. Continuum dynamics of the 1-D Heisenberg antiferromagnet: identification with the O(3) nonlinear sigma model. *Phys. Lett. A* **1983**, *93*, 464–468.
- [20] den Nijs, M.; Rommelse, K. Preroughening transitions in crystal surfaces and valence-bond phases. *Phys. Rev. B* **1989**, *40*, 4709–4734.
- [21] Li, H.; Haldane, F. D. M. Entanglement spectrum as a generalization of entanglement entropy: identification of topological order in non-Abelian fractional quantum Hall effect states. *Phys. Rev. Lett.* **2008**, *101*, 010504.
- [22] Zak, J. Berry’s phase for energy bands in solids. *Phys. Rev. Lett.* **1989**, *62*, 2747–2750.
- [23] Resta, R. Quantum-mechanical position operator in extended systems. *Phys. Rev. Lett.* **1998**, *80*, 1800–1803.
- [24] Pollmann, F.; Turner, A. M.; Berg, E.; Oshikawa, M. Entanglement spectrum of a topological phase in one dimension. *Phys. Rev. B* **2010**, *81*, 064439.
- [25] Barnes, T.; Riera, J.; Tennant, D. A. A Study of the $S = 1/2$ Alternating Chain using Multiprecision Methods. *Phys. Rev. B* **1999**, *59*, 11384–11397.
- [26] Harris, A. B. Alternating Linear Heisenberg Antiferromagnet: The Exciton Limit. *Phys. Rev. B* **1973**, *7*, 3166–3187.
- [27] Bonner, J. C.; Blöte, H. W. J. Excitation spectra of the linear alternating antiferromagnet. *Phys. Rev. B* **1982**, *25*, 6959–6980.
- [28] White, S. R.; Affleck, I. Spectral function for the $S = 1$ Heisenberg antiferromagnetic chain. *Phys. Rev. B* **2008**, *77*, 134437.
- [29] Maeda, Y.; Hotta, C.; Oshikawa, M. Universal Temperature Dependence of the Magnetization of Gapped Spin Chains. *Phys. Rev. Lett.* **2007**, *99*, 057205.
- [30] Tersoff, J.; Hamann, D. R. Theory and Application for the Scanning Tunneling Microscope. *Phys. Rev. Lett.* **1983**, *50*, 1998–2001.
- [31] White, S. R. Density matrix formulation for quantum renormalization groups. *Phys. Rev. Lett.* **1992**, *69*, 2863–2866.
- [32] Xiang, H.; Lee, C.; Koo, H.-J.; Gong, X.; Whangbo, M.-H. Magnetic properties and energy-mapping analysis. *Dalton Trans.* **2013**, *42*, 823–853.

- [33] Meng, Z. Y.; Lang, T. C.; Wessel, S.; Asaad, F. F.; Muramatsu, A. Quantum spin liquid emerging in two-dimensional correlated Dirac fermions. *Nature* **2010**, *464*, 847–851.
- [34] Anindya, K. N.; Rochefort, A. Controlling the magnetic properties of two-dimensional carbon-based Kagome polymers. *Carbon Trends* **2022**, *7*, 100170.
- [35] Kim, J.; Kim, J.; Kim, J.; Lee, J.; Park, Y.; Kang, Y.; Han, S. Data-Efficient Multifidelity Training for High-Fidelity Machine Learning Interatomic Potentials. *Journal of the American Chemical Society* **2025**, *147*, 1042–1054.
- [36] Park, Y.; Kim, J.; Hwang, S.; Han, S. Scalable Parallel Algorithm for Graph Neural Network Interatomic Potentials in Molecular Dynamics Simulations. *Journal of Chemical Theory and Computation* **2024**, *20*, 4857–4868.
- [37] Anindya, K. N.; Guo, H. Moiré-induced fragile topology and Chern bands in twisted organic kagome bilayers. *Phys. Rev. B* **2025**, *112*, 155160.
- [38] Auerbach, A. *Interacting Electrons and Quantum Magnetism*; Springer: New York, 1994.
- [39] Gandon, A.; Baiardi, A.; Rossmannek, M.; Dobrautz, W.; Tavernelli, I. Quantum Computing in Spin-Adapted Representations for Efficient Simulations of Spin Systems. *PRX Quantum* **2025**, *6*, 030306.
- [40] Hirjibehedin, C. F.; Lutz, C. P.; Heinrich, A. J. Spin Coupling in Engineered Atomic Structures. *Science* **2006**, *312*, 1021–1024.
- [41] Lovesey, S. W. *Theory of Neutron Scattering from Condensed Matter*; Oxford University Press: Oxford, 1984.
- [42] Cococcioni, M.; de Gironcoli, S. Linear response approach to the calculation of the effective interaction parameters in the LDA + U method. *Phys. Rev. B* **2005**, *71*, 035105.

Acknowledgements

This work was supported by the Natural Sciences and Engineering Research Council of Canada (NSERC) and Fonds de recherche du Québec – Nature et technologies (FRQNT) and would have not been possible without the computational resources provided by Calcul Québec and the Digital Research Alliance of Canada (The Alliance).

Supporting information

The Supporting Information is available free of charge at

Model symmetries and numerical methods for the spin-chain calculations (Section S1); DFT+ U setup and extraction of exchange parameters for the spin- $\frac{1}{2}$ and Hund-coupled spin-1 chains (Section S2); finite-temperature molecular dynamics and construction of time-averaged structures (Section S3); and 300 K structural stability diagnostics (Section S4; Supporting Figure S1).

Supporting Information for: *Tunable Topological Phases in an Organic One-Dimensional Mott Chain: Odd-Haldane ($S = 1/2$) and Haldane ($S = 1$)*

Khalid N. Anindya^{*1} and Hong Guo¹

¹Department of Physics, McGill University, Montréal, QC H3A 2T8, Canada

^{*}Email: khalid.anindya@mcgill.ca

S1. Model symmetries and numerical methods

S1.1 SU(2) symmetry and sector structure

The spin model used in the main text is the isotropic, nearest-neighbor Heisenberg chain with alternating couplings [Eq. (1) in main text]. At zero magnetic field this Hamiltonian is fully SU(2) symmetric: it commutes with the components of the total spin $\hat{\mathbf{S}}_{\text{tot}} = \sum_i \hat{\mathbf{S}}_i$ and with $\hat{\mathbf{S}}_{\text{tot}}^2$, so eigenstates can in principle be labeled by (S, S^z) .

In both our exact-diagonalization (ED) and DMRG calculations we exploit the U(1) subgroup generated by \hat{S}_{tot}^z . The Hilbert space is decomposed into blocks with fixed S_{tot}^z , and the many-body problem is solved independently in each block. The full SU(2) structure is then used a posteriori: for low-lying eigenstates $|\psi_n\rangle$ we compute $\langle \hat{\mathbf{S}}_{\text{tot}}^2 \rangle_n$ and check that they cluster near $S(S+1)$ with $S = 0, 1, \dots$, confirming the expected singlet, triplet, etc. multiplets and their near degeneracies. This is particularly important for identifying the Haldane phase, where the ground state in the bulk is a singlet but the open chain exhibits emergent $S = 1/2$ edge degrees of freedom.

Whenever we probe a finite magnetic field B along z we add the Zeeman term $-g\mu_B B \sum_i \hat{S}_i^z$ on top of Eq. (1). This breaks SU(2) down to U(1), but \hat{S}_{tot}^z remains conserved so the block structure is unchanged. The field simply splits the SU(2) multiplets in the expected way and can be used to identify level crossings and saturation fields.

S1.2 ED for the strongly dimerized spin- $\frac{1}{2}$ chain

For the “odd-Haldane” spin-1/2 realization relevant to the nanographene spin chains, the mapping from DFT yields a very strongly dimerized limit: the weak coupling J_1 is effectively vanishing ($J_1 \approx 0$) while the strong coupling $J_2 > 0$ sets the main energy scale. Physically, this corresponds to almost perfect dimers weakly coupled into a chain. The correlation length is then very short, of order a couple of sites, so finite-size effects decay rapidly with chain length.

In this regime we treat the system entirely with exact diagonalization:

- We work with an open chain of $N = 12$ spin-1/2 sites. Here one spin-1/2 site corresponds to one nanographene monomer, so $N = 12$ corresponds to a chain of 12 monomers.
- The Hilbert space dimension is $2^{12} = 4096$, which allows us to construct the full Hamiltonian of Eq. (1) in sparse-matrix form in each S_{tot}^z sector and diagonalize it using Lanczos (or Arnoldi) routines. We typically target the lowest few eigenstates in each block.
- We use open boundary conditions with the same alternating bond pattern as in the real chain. The edges cut through a weak bond, leaving the strong (dimer) bonds just inside the chain and exposing fractionalized $S = 1/2$ edge degrees of freedom.

- The ground state is obtained in the lowest- $|S_{\text{tot}}^z|$ sector ($S_{\text{tot}}^z = 0$ at $B = 0$). Excited states in $S_{\text{tot}}^z = \pm 1$ are used to define bulk and edge triplet gaps.

Because numerical diagonalization in $S_{\text{tot}}^z = 0$ does not by itself enforce any constraint on the spatial distribution of $\langle \hat{S}_i^z \rangle$, we additionally symmetrize the ground state with respect to a global π rotation around the x axis, $\hat{F} = \bigotimes_i \hat{\sigma}_i^x$ (where $\hat{\sigma}_i^x$ is the Pauli matrix acting on site i). Given a numerically obtained $S_{\text{tot}}^z = 0$ eigenvector $|\psi\rangle$, we form $|\psi_{\pm}\rangle \propto (|\psi\rangle \pm \hat{F}|\psi\rangle)$ and pick the lower-energy parity sector. This projection enforces $\langle \hat{S}_i^z \rangle \equiv 0$ in the bulk Haldane region of the spin-1/2 chain and makes the emergence of edge magnetization near the boundaries much cleaner.

From these ED calculations on $N = 12$ we extract:

1. The bulk triplon gap and dispersion bandwidth (via the lowest $S_{\text{tot}}^z = \pm 1$ excitations on a ring; see below).
2. The open-chain edge gap (difference between the lowest singlet and lowest triplet for the same S_{tot}^z).
3. Real-space spin densities $\langle \hat{S}_i^z \rangle$, which show the fractionalized edge spins and their decay into the bulk.
4. The spectrum of low-lying states as a function of S_{tot}^z , which we organize into multiplets using $\langle \hat{\mathbf{S}}_{\text{tot}}^z \rangle$.

We verified that increasing the chain length to $N = 14$ and $N = 16$ in the same dimerized regime does not modify the gaps significantly. Thus, $N = 12$ monomers already behaves as an effectively infinite chain for the spin-1/2 case.

S1.3 Periodic chain, triplon dispersion, and $S^{+-}(q, \omega)$

To access momentum-resolved information we also consider the periodic version of the chain. On a ring we implement boundary conditions and “twists” by modifying the bond between the last and first sites in Eq. (1). A twist angle ϕ is introduced on the wrap bond in the transverse exchange part, so that the many-body ground state and lowest $S_{\text{tot}}^z = \pm 1$ excitations can be followed as a function of ϕ . We use the boundary twist ϕ as a continuous proxy for the crystal momentum in the reduced (two-site) Brillouin zone, folding k into $0 \leq k \leq \pi$. Here k labels the dispersion extracted from twisted boundary conditions, while $q \in [0, 2\pi)$ is the wavevector used in $S^{+-}(q, \omega)$ on the site lattice.

For each twist angle we compute:

- The ground-state energy $E_0(\phi)$ in the sector with smallest $|S_{\text{tot}}^z|$ (typically $S_{\text{tot}}^z = 0$).
- The lowest excitation $E_1^{(+)}(\phi)$ in the sector $S_{\text{tot}}^z = +1$.

The one-triplon dispersion is then defined as

$$E_{\text{bulk}}(k) = E_1^{(+)}(\phi) - E_0(\phi), \quad k \equiv \phi. \quad (1)$$

This is what we compare to the dominant ridge in the dynamical structure factor $S^{+-}(q, \omega)$ and to analytical expectations based on the strong-dimer (triplon) description of the alternating-exchange chain and effective Haldane chain.

For the dynamical spin structure factor itself, we evaluate

$$S^{+-}(q, \omega) = \frac{1}{\pi} \sum_n \left| \langle n | \hat{S}_q^+ | 0 \rangle \right|^2 \frac{\eta}{[\omega - (E_n - E_0)]^2 + \eta^2}, \quad (2)$$

where $|0\rangle$ is the ground state at $\phi = 0$, $\hat{S}_q^+ = N^{-1/2} \sum_j e^{-iqj} (\hat{S}_j^x + i\hat{S}_j^y)$ is the Fourier-transformed spin-raising operator, and η is a small broadening. Numerically, this is implemented with a Lanczos continued-fraction method starting from the initial state $|\phi_q\rangle = \hat{S}_q^+ |0\rangle$. The Krylov subspace generated by successive actions of the Hamiltonian is tridiagonalized, and the continued fraction for the local Green’s function is evaluated on a grid of ω . In practice we use on the order of 10^2 – 10^3 Lanczos iterations, a uniform grid of q values in $[0, 2\pi)$, and a broadening η of order 0.5–1 meV. The resulting intensity maps are lightly smoothed along the energy axis and used to extract the ridge that defines the triplon band in the main text.

S1.4 DMRG for the Hund-coupled spin-1 chain

The ‘‘Haldane chain’’ realized in the nanographene $S = 1$ platform is not a chain of ideal spin-1 atoms, but a chain of Hund-coupled superatoms: each monomer hosts two spin-1/2 sites, coupled ferromagnetically by a large $J_1 < 0$, and neighboring monomers are coupled antiferromagnetically by $J_2 > 0$ with $|J_1| \gg J_2$. In the limit $|J_1| \rightarrow \infty$ each monomer would form an exact $S = 1$ unit, but at realistic J_1 the local moment is slightly ‘‘soft’’ and the correlation length is enhanced relative to the ideal spin-1 chain.

To capture this realistic spin-1 Haldane physics we need substantially larger systems than are accessible to ED. We therefore use DMRG¹ as implemented in the TenPy library,² working with chains of

$$N_{\text{sites}} = 32$$

spin-1/2 sites grouped into 16 monomers (two sites per monomer). In the effective spin-1 description this corresponds to a chain of $N_{S=1} = 16$ sites.

The main features of the DMRG setup are:

- We retain the U(1) symmetry associated with conservation of S_{tot}^z . The MPS tensors therefore carry a U(1) ‘‘charge’’ and the Hilbert space is block-sparse, which greatly improves efficiency. Non-Abelian SU(2) is not enforced at the tensor-network level, but we again verify that the low-energy spectrum organizes into approximate SU(2) multiplets via $\langle \hat{\mathbf{S}}_{\text{tot}}^2 \rangle$.
- We use open boundary conditions and the same alternating bond pattern as in the real Hund chain: strong ferromagnetic J_1 bonds within each monomer and antiferromagnetic J_2 bonds between monomers. This produces the expected Haldane edge states, whose spatial profiles are extended across several physical sites near each end.
- We perform finite-system DMRG sweeps, increasing the maximum bond dimension up to $\chi \sim 10^3$ and converging the truncation error to $\epsilon_{\text{trunc}} \leq 10^{-8}$ for the ground state. Convergence is checked by monitoring the energy, entanglement entropy and local observables as functions of sweep number and χ .

From the converged MPS we obtain:

1. The bulk Haldane gap, by targeting the lowest state in the lowest- $|S_{\text{tot}}^z|$ sector and the lowest state in $S_{\text{tot}}^z = \pm 1$, taking their energy difference and extrapolating in the centre of the chain.
2. The edge magnetization profile $\langle \hat{S}_i^z \rangle$, which shows the emergent fractionalized edge spins and their exponential decay into the bulk. Fitting this decay yields a correlation length ξ that is a couple monomers long.
3. The entanglement spectrum across a cut in the middle of the chain. The even-fold degeneracy of the Schmidt values provides a robust diagnostic of the Haldane SPT phase and is consistent with the edge and bulk gap analysis.

Test runs at $N_{\text{sites}} = 40$ (20 monomers) show that bulk quantities (gap, entanglement spectrum, central $\langle \hat{S}_i^z \rangle$) are indistinguishable from the $N_{\text{sites}} = 32$ results within numerical accuracy. We therefore use $N_{\text{sites}} = 32$ as our standard system size for the Hund-coupled spin-1 chain.

S1.5 Many-body Zak phase and string order parameter

For completeness, we have implemented standard SPT diagnostics such as the many-body Zak (Berry) phase and the nonlocal string order parameter. We determined Zak-phase based on inserting a global twist ϕ on the ring and following the many-body ground state $|\psi_0(\phi)\rangle$ along a closed loop $0 \leq \phi < 2\pi$. The many-body Zak (Berry) phase is obtained from the discretized Berry connection

$$\gamma_{\text{Zak}} = -\text{Im} \sum_j \ln \frac{\langle \psi_0(\phi_j) | \psi_0(\phi_{j+1}) \rangle}{|\langle \psi_0(\phi_j) | \psi_0(\phi_{j+1}) \rangle|}, \quad (3)$$

which is quantized to 0 or $\pi \pmod{2\pi}$ in the presence of the protecting symmetries and cleanly distinguishes the topologically trivial and Haldane phases. In addition to the results shown in main manuscript, we have also computed the nonlocal string order parameter which is evaluated directly from ED and DMRG, and shows the expected finite value in the SPT regime and its collapse upon tuning to the trivial phase. These quantities are fully consistent with the edge/bulk gap diagnostics above and provide an independent many-body confirmation of the interacting SPT phase.

S1.6 Consistency between ED and DMRG

The ED and DMRG calculations address complementary regimes of the same effective spin model. For the strongly dimerized spin- $\frac{1}{2}$ chain ($J_1 \approx 0$) ED on $N = 12$ monomers is essentially exact and provides unbiased access to the full low-energy spectrum, edge gaps, triplon bandwidth, and real-space spin profiles. In this regime the correlation length is so short that increasing the system size to $N = 14$ or $N = 16$ has a negligible effect, indicating that ED already represents the thermodynamic limit.

For the Hund-coupled spin-1 chain, an exponential fit of the edge gap vs chain length yields a correlation length $\xi \approx 4$ spin- $\frac{1}{2}$ sites ≈ 2 Hund monomers; the edge spins thus decay over only a few monomers. To obtain a clean bulk region and essentially decoupled edges we therefore simulate chains of 32 spin- $\frac{1}{2}$ sites (16 monomers), which is beyond the reach of ED and is treated with DMRG (TenPy) exploiting U(1) symmetry. Here DMRG on $N_{\text{sites}} = 32$ (16 monomers) provides accurate bulk gaps, entanglement spectra, and edge profiles. In parameter regimes where both methods are feasible (e.g. reduced $|J_1|$ and shorter chains), we find that ED and DMRG yield consistent gaps and local observables within numerical accuracy. This cross-check supports the use of ED for the spin- $\frac{1}{2}$ chain and DMRG for the Hund-coupled spin-1 chain as reliable and mutually consistent descriptions of the interacting SPT phases discussed in the main text.

S2. DFT+ U calculations and extraction of exchange parameters

S2.1 DFT+ U setup

All electronic-structure calculations are performed within spin-polarized DFT+ U using the PBE generalized-gradient approximation as implemented in the QUANTUM ESPRESSO package.^{3,4} Such DFT+ U approaches have been validated previously for related systems.^{5,6} The interaction between valence electrons and ionic cores is described by projector-augmented wave (PAW) datasets.⁷

The unit cells of the CTP-based chains contain 64 atoms (including hydrogen terminations). All structures are fully relaxed until the total-energy change is smaller than 10^{-7} Ry and the residual forces on each atom are below 10^{-6} Ry/Å. Structural optimizations are carried out on a Γ -centered $8 \times 1 \times 1$ k -point mesh, with a plane-wave kinetic-energy cutoff of 50 Ry. A vacuum spacing of 20 Å is used along the out-of-plane (z) direction to avoid spurious interactions between periodic images. All spin-polarized calculations assume collinear magnetism with the spin quantization axis aligned along z for simplicity.

For accurate band structures and density of states we use a denser $30 \times 1 \times 1$ k -point mesh on the relaxed geometries.

S2.2 Linear-response Hubbard U on C, N, and O sites

The Hubbard corrections in our DFT+ U calculations are applied to the $2p$ shells of the C, N, and O atoms that belong to the π -conjugated backbone and carbonyl groups of the CTP framework. The corresponding on-site interaction parameters U_α (with $\alpha = \text{C, N, O}$) are obtained from first-principles linear-response theory following the Cococcioni and de Gironcoli scheme.⁸ We use the implementation provided in the QUANTUM ESPRESSO distribution.

In this approach, one introduces a small on-site potential shift δV_α on the localized orbital manifold of a given atomic species (e.g. the $2p$ subspace of a particular carbon site) and computes the induced change in the corresponding occupation numbers n_α . From these we construct the bare and screened response matrices,

$$\chi_{\alpha\beta}^0 = \left. \frac{\partial n_\alpha}{\partial V_\beta} \right|_{\text{KS}}, \quad \chi_{\alpha\beta} = \left. \frac{\partial n_\alpha}{\partial V_\beta} \right|_{\text{SCF}},$$

where α, β run over all symmetry-inequivalent Hubbard sites in the unit cell. The effective Hubbard matrix is then obtained as

$$U_{\alpha\beta} = \left(\chi^{0^{-1}} - \chi^{-1} \right)_{\alpha\beta},$$

and the on-site U_α entering the DFT+ U functional is taken as the diagonal element $U_{\alpha\alpha}$, averaged over symmetry-equivalent atoms. In practice we find that the off-diagonal elements are small and that U_α is nearly site-independent within each chemical species, so we use a single U_C , U_N , and U_O for all equivalent backbone and carbonyl sites.⁶

This procedure is particularly important for the carbonyl O $2p$ states, whose self-interaction errors strongly influence the local moment on the adjacent CTP backbone and the magnitude of the exchange splitting. With the linear-response U values, the DFT+ U band structures correctly recover the open-shell character and the magnitude of the experimental spin splittings reported for related systems.⁶

S2.3 Mapping collinear DFT+ U energies to J_1, J_2 : spin- $\frac{1}{2}$ alternating-exchange chain

For the spin-1/2 alternating-exchange chain the low-energy physics is captured by two antiferromagnetic couplings $J_1, J_2 > 0$ along the polymer backbone. Each monomer hosts a single localized spin-1/2 moment, and the effective one-dimensional Heisenberg model [Eq. (1)] contains two distinct nearest-neighbor bonds per unit cell.

To extract J_1 and J_2 we construct a four-site supercell containing two unit cells of the spin chain. We then compute DFT+ U total energies for a set of collinear spin configurations, chosen such that each bond is sampled in both ferromagnetic (FM) and antiferromagnetic (AFM) alignments. A convenient choice is:

$$\begin{aligned} \text{FM} &: \uparrow\uparrow \mid \uparrow\uparrow, \\ \text{AFM-1} &: \uparrow\downarrow \mid \uparrow\downarrow, \\ \text{AFM-2} &: \uparrow\uparrow \mid \downarrow\downarrow, \end{aligned}$$

where the vertical bar separates the two original unit cells. In a classical Ising approximation to the Heisenberg model, each bond contributes an energy $J_{ij} \langle \mathbf{S}_i \cdot \mathbf{S}_j \rangle$, with $\langle \mathbf{S}_i \cdot \mathbf{S}_j \rangle = +\frac{1}{4}$ for parallel spins and $-\frac{1}{4}$ for antiparallel spins. Writing the DFT energies for the three configurations as E_{FM} , $E_{\text{AFM-1}}$, and $E_{\text{AFM-2}}$, and counting how many J_1 and J_2 bonds are parallel or antiparallel in each configuration yields a linear system of the form

$$E_{\text{FM}} = E_0 + a_1 J_1 + a_2 J_2, \quad (4)$$

$$E_{\text{AFM-1}} = E_0 + b_1 J_1 + b_2 J_2, \quad (5)$$

$$E_{\text{AFM-2}} = E_0 + c_1 J_1 + c_2 J_2, \quad (6)$$

where E_0 is a spin-independent reference energy and the coefficients a_i, b_i, c_i are simple rational numbers proportional to $\pm\frac{1}{4}$. Eliminating E_0 and solving for J_1 and J_2 gives the desired exchange constants.

In our nanographene spin-1/2 chain, this mapping yields a very weak J_1 and a much larger J_2 , i.e. $J_1 \simeq 0$ and $J_2 > 0$, placing the system extremely close to the limit of isolated dimers. This is the parameter regime used in the ED calculations for the ‘‘odd-Haldane’’ spin-1/2 phase.

S2.4 Mapping collinear DFT+ U energies to Hund exchange and inter-monomer J_1, J_2 : spin-1 chain

For the effective spin-1 chain, the building blocks are Hund-coupled superatoms: each nanographene monomer hosts two spin- $\frac{1}{2}$ sites, coupled ferromagnetically by a large intra-monomer exchange $J_1 < 0$, while neighboring monomers are coupled antiferromagnetically by $J_2 > 0$. In the spin-1 description these correspond to the intra- and inter-monomer bonds of the Heisenberg chain in Eq. (1).

In practice we do not extract J_1 and J_2 from separate ‘‘isolated monomer’’ and ‘‘two-monomer’’ calculations. Instead we use exactly the same four-site mapping as for the spin- $\frac{1}{2}$ alternating chain, but now the four spin- $\frac{1}{2}$ sites belong to a single crystallographic unit cell containing two monomers,

$$A \equiv (1, 2), \quad B \equiv (3, 4),$$

with J_1 bonds inside each monomer (1–2 and 3–4) and J_2 bonds connecting the monomer A to monomer B along the backbone. All symmetry-equivalent J_2 bonds within the unit cell are assumed equal.

We evaluate DFT+ U total energies for the following three collinear spin configurations of the four sites,

$$\begin{aligned} \text{FM} &: \uparrow\uparrow \mid \uparrow\uparrow, \\ \text{AFM-1} &: \uparrow\downarrow \mid \uparrow\downarrow, \\ \text{AFM-2} &: \uparrow\uparrow \mid \downarrow\downarrow, \end{aligned}$$

where the vertical bar again separates monomer A from monomer B . In each pattern, every J_1 and J_2 bond is either parallel or antiparallel, so its contribution to the Heisenberg energy can be written as $J \langle \mathbf{S}_i \cdot \mathbf{S}_j \rangle$ with $\langle \mathbf{S}_i \cdot \mathbf{S}_j \rangle = +\frac{1}{4}$ for parallel spins and $-\frac{1}{4}$ for antiparallel spins.

Denoting the DFT+ U total energies of these three configurations by E_{FM} , $E_{\text{AFM-1}}$ and $E_{\text{AFM-2}}$, and counting how many J_1 and J_2 bonds are parallel or antiparallel in each case, we obtain the same algebraic mapping as in Sec. S2.3 for the spin- $\frac{1}{2}$ chain: the three equations are sufficient to eliminate E_0 and solve uniquely for J_1 and J_2 .

The crucial difference lies in the resulting parameter regime and its physical interpretation. For the spin- $\frac{1}{2}$ chain we obtain two antiferromagnetic couplings $J_1, J_2 > 0$ with $J_1 \simeq 0$ and $J_2 > 0$, corresponding to an almost perfectly dimerized AFM chain. For the Hund-coupled spin-1 chain, applying the same four-site mapping to the unit cell yields

$$J_1 < 0, \quad J_2 > 0, \quad |J_1| \gg J_2,$$

i.e. a large ferromagnetic intra-monomer Hund exchange J_1 that locks the two spin- $\frac{1}{2}$ sites within each monomer into an effective $S = 1$ superatom, and a weaker antiferromagnetic inter-monomer exchange J_2 that couples neighboring $S = 1$ superatoms along the chain. In the notation of the main text we therefore identify

$$J_1 = J_{\text{FM}} \quad (\text{intra-monomer Hund exchange}), \quad J_2 = J_{\text{AFM}} \equiv J_{\text{eff}} \quad (\text{inter-monomer AFM exchange}).$$

These J_1 and J_2 values are the ones used as input for the ED and DMRG calculations of the interacting Haldane spin-1 chain in the main text.

S3. Finite-Temperature Molecular Dynamics and Time-Averaged Structures

S3.1 MD setup

Classical molecular dynamics (MD) was performed with LAMMPS⁹ using the fine-tuned SevenNet-MF-OMPA machine-learning interatomic potentials.^{10–12} The simulation cell is quasi-one-dimensional with periodic boundary conditions only along the chain direction (`boundary p f f`). The 0 K relaxed structure served as the starting geometry. All simulations employed metal units, a time step of $\Delta t = 0.0005$ ps (0.5 fs), velocity-Verlet integration, a neighbor skin of 2.0 Å rebuilt every step, and linear center-of-mass momentum removal every 100 steps. Parallel domain decomposition was aligned with the chain axis and dynamically load-balanced.

S3.2 Stage I: anisotropic barostat (NPT- x) to obtain the stress-free repeat length $L_x^*(T)$

At a target temperature T , we relaxed only the periodic lattice length using an anisotropic Nosé–Hoover thermostat/barostat:^{13–15}

The thermostat damping time was 0.2 ps and the barostat damping time along x was 8.0 ps, with additional barostat drag (1.5) to suppress ringing. The total NPT- x duration was $t_{\text{NPT}} = 40$ ps, split into a *settle* window of 25 ps (not averaged) followed by an *average* window of 15 ps. Over the average window

we recorded the scalar averages

$$L_x^*(T) = \langle L_x \rangle \equiv \frac{1}{N_{\text{avg}}} \sum_{k=1}^{N_{\text{avg}}} L_x(k), \quad (7)$$

$$\sigma(L_x) = \sqrt{\langle L_x^2 \rangle - \langle L_x \rangle^2}, \quad \langle P_{xx} \rangle = \frac{1}{N_{\text{avg}}} \sum_{k=1}^{N_{\text{avg}}} P_{xx}(k), \quad (8)$$

using time-averaging fixes. Because the cell is non-periodic in y, z , instantaneous P_{xx} exhibits large fluctuations; the zero-tension criterion is therefore based on the long-time mean $\langle P_{xx} \rangle$ together with the observed plateau of $L_x(t)$. After NPT- x , the box length was set to the averaged value $L_x^*(T)$ via a `change_box` operation (preserving x_{lo}).

S3.3 Stage II: NVT at fixed $L_x = L_x^*(T)$ and time-averaged geometry

With L_x fixed to $L_x^*(T)$, we ran a Nosé-Hoover NVT at the same temperature:

The NVT stage comprised a 10 ps settle segment followed by a 20 ps production segment. During production we accumulated arithmetic mean atomic coordinates with a per-atom time-averaging fix to obtain

$$\bar{\mathbf{r}}_i = \frac{1}{N_{\text{prod}}} \sum_{k=1}^{N_{\text{prod}}} \mathbf{r}_i(k), \quad i = 1, \dots, N_{\text{atoms}}, \quad (9)$$

and monitored $L_x(t)$ to confirm stability at $L_x^*(T)$. A trajectory was written every 1000 steps for distributional analyses (bond/angle/dihedral and transverse fluctuations), and an instantaneous end-of-run snapshot and restart were saved for reproducibility.

S3.4 Thermal expansion and uncertainties

Repeating the above at several temperatures yields $L_x^*(T)$ versus T . The one-dimensional linear thermal expansion coefficient is obtained by a linear fit,

$$\alpha \equiv \frac{1}{L_x^*(0)} \frac{dL_x^*(T)}{dT}, \quad (10)$$

with uncertainties estimated from the standard errors of $L_x^*(T)$ over the NPT- x averaging windows and propagated through the fit.

All numerical parameters (damping times, settle/average durations, and dump cadences) match those used in production and were chosen to suppress barostat ringing in the quasi-1D geometry while providing statistically converged late-time averages.

S4. Finite-Temperature Molecular Dynamics: 300 K Structural Stability

S4.1 Unified interpretation (applies to both chains)

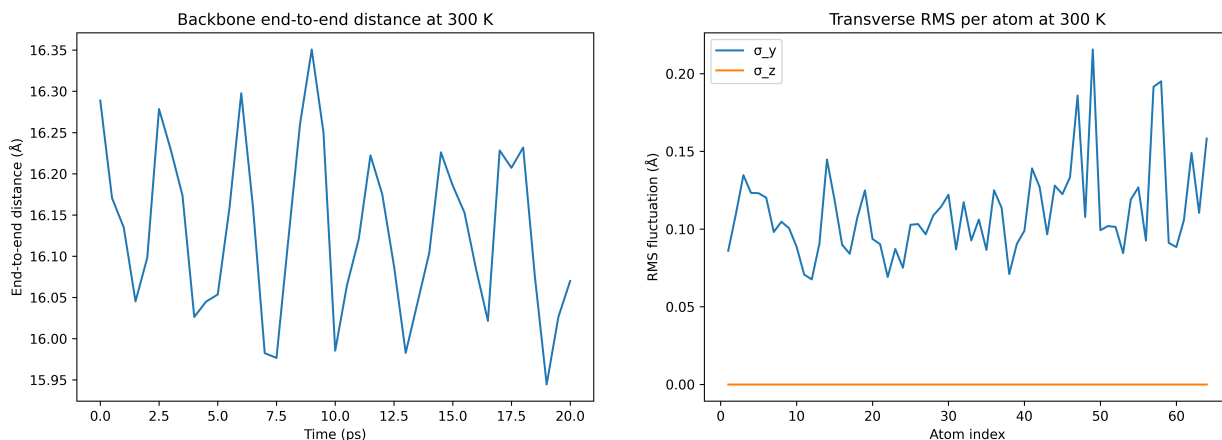
Two complementary diagnostics summarize the 300 K structural response under periodicity along the chain axis. (i) The end-to-end trace (minimum-image disabled; both termini kept in the same box image) is a stability check: a narrow, stationary band indicates a stress-balanced repeat length and the absence of creep, progressive buckling, or slow uncoiling on the simulated timescale. (ii) The transverse RMS profile provides a flexibility map: peaks at inter-monomer linkages and substituents identify hinge-like regions, whereas valleys on aromatic carbons mark a stiff conjugated backbone. Out-of-plane fluctuations remain near the numerical floor, consistent with an essentially planar geometry at 300 K.

S4.2 Chain-specific notes

Spin- $\frac{1}{2}$ chain. The end-to-end distance forms a tight, stationary band (mean ≈ 16.13 Å, s.d. ≈ 0.10 Å over the production window). The transverse RMS highlights localized flexibility at junctions and side groups while the aromatic cores remain rigid in-plane. **Spin-1 chain.** The end-to-end trace is likewise stationary with small-amplitude thermal modulations (mean ≈ 16.14 Å, s.d. ≈ 0.04 Å). The transverse RMS exhibits the same qualitative pattern—enhanced motion at junctions/substituents; near-zero out-of-plane fluctuations—confirming preserved planarity at 300 K.

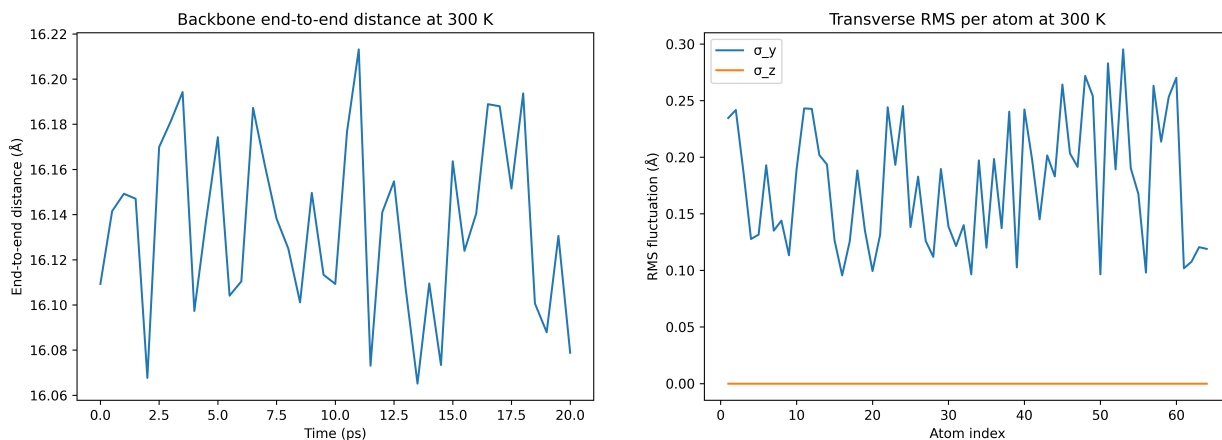
S4.3 Implications

Both chains maintain a well-defined, planar backbone at 300 K, with thermal motion concentrated at chemically sensible soft spots. This supports the use of a single, temperature-specific geometry and modest fluctuation envelopes for subsequent electronic and magnetic analyses.



(a) Spin- $\frac{1}{2}$: end-to-end distance at 300 K. Stationary, narrowly distributed trace indicating a stress-balanced repeat length.

(b) Spin- $\frac{1}{2}$: transverse RMS per atom at 300 K. Flexibility localizes at junctions and substituents; the aromatic backbone remains rigid and essentially planar.



(c) Spin-1: end-to-end distance at 300 K. Narrow, drift-free band consistent with a stress-balanced repeat length.

(d) Spin-1: transverse RMS per atom at 300 K. Junction-localized flexibility with near-zero out-of-plane motion; backbone remains planar.

Figure S1: Structural stability diagnostics at 300 K for the spin- $\frac{1}{2}$ and spin-1 chains. End-to-end traces serve as stability checks; transverse RMS profiles map flexibility along the backbone.

References

- [1] White, S. R. *Phys. Rev. Lett.* **1992**, *69*, 2863–2866.
- [2] Hauschild, J.; Pollmann, F. *SciPost Phys. Lect. Notes* **2018**, *5*.
- [3] Giannozzi, P. et al. *Journal of Physics: Condensed Matter* **2009**, *21*, 395502.
- [4] Giannozzi, P. et al. *Journal of Physics: Condensed Matter* **2017**, *29*, 465901.
- [5] Anindya, K. N.; Rochefort, A. *Carbon Trends* **2022**, *7*, 100170.
- [6] Pawlak, R.; Anindya, K. N.; Chahib, O.; Liu, J.-C.; Hiret, P.; Marot, L.; Luzet, V.; Palmino, F.; Chérioux, F.; Rochefort, A.; Meyer, E. *ACS Nano* **2025**, *19*, 4768–4777.
- [7] Blöchl, P. E. *Phys. Rev. B* **1994**, *50*, 17953–17979.
- [8] Cococcioni, M.; de Gironcoli, S. *Phys. Rev. B* **2005**, *71*, 035105.
- [9] Plimpton, S. *Journal of Computational Physics* **1995**, *117*, 1–19.
- [10] Kim, J.; Kim, J.; Kim, J.; Lee, J.; Park, Y.; Kang, Y.; Han, S. *Journal of the American Chemical Society* **2025**, *147*, 1042–1054.
- [11] Park, Y.; Kim, J.; Hwang, S.; Han, S. *Journal of Chemical Theory and Computation* **2024**, *20*, 4857–4868.
- [12] Anindya, K. N.; Guo, H. *Phys. Rev. B* **2025**, *112*, 155160.
- [13] Nosé, S. *The Journal of Chemical Physics* **1984**, *81*, 511–519.
- [14] Hoover, W. G. *Physical Review A* **1985**, *31*, 1695–1697.
- [15] Martyna, G. J.; Klein, M. L.; Tuckerman, M. *The Journal of Chemical Physics* **1992**, *97*, 2635–2643.